Rock Mechanics and Rock Engineering (2023) 56:1717–1737
https://doi.org/10.1007/s00603-022-03144-8

ORIGINAL PAPER

Experimental and Numerical Study on Shear Behaviors of Rock Joints Reinforced by SFCBs and BFRP Bars

Shubo Zhang[1] · Changsheng Wang[1] · Gang Wang[1,2] · Xin Zheng[1] · Hui Guan[1] · Tingfang Liu[1] · Feng Xu[1]

Received: 6 April 2022 / Accepted: 25 October 2022 / Published online: 27 November 2022
© The Author(s), under exclusive licence to Springer-Verlag GmbH Austria, part of Springer Nature 2022

Abstract

To study the shear behaviors of jointed rocks reinforced by basalt fiber-reinforced polymer (BFRP) bars and steel–FRP composite bars (SFCBs), we conduct laboratory tests and numerical simulations to analyze the shear strength, shear stiffness, energy dissipation, and bolt failure modes. Our results show that the shear stiffness of the BFRP bolted specimen is lower than that of the specimens bolted by steel bars and SFCBs, but the residual shear strength is higher. SFCB-reinforced jointed rock has the highest peak shear strength, and its residual strength is similar to that of the steel bar bolted specimen. The total energy absorbed by the BFRP bolted specimen is comparable to that absorbed by the steel bolted specimen. When the bolt inclination angle is 60°, the shear strength of the BFRP bar bolted specimens is higher than that of the steel reinforced one. The failure characteristics of BFRP bar bolted rocks can be categorized as resin matrix fracture, resin matrix and fiber shear, and fracture of resin matrix and rocks. The failure modes of the SFCB divided into surface FRP failure and steel bending. Based on numerical results, BFRP bars have larger axial force than conventional bolts, but lower shear stress. The axial stress of the BFRP bar increases as the bolt inclination angle decreases. Moreover, the BFRP bar is more likely to cause shear cracks at the interface between the rock and the bolt.

Highlights

- Experimental and numerical tests were conducted on the jointed specimens reinforced by Basalt Fiber Reinforced Polymer bar and Steel-FRP composite bar.
- In terms of shear stiffness and residual shear strength, the jointed specimen reinforced by Basalt Fiber Reinforced Polymer bar and Steel-FRP composite bar differ significantly from steel.
- The specimens reinforced by Basalt Fiber Reinforced Polymer bar are sensitive to the effect of the bolt inclination angles and have higher shear strengths than conventional bolts at the bolt inclination angle is 60°.
- The axial force and shear force variation laws of different types of bolts were discovered.

Keywords BFRP bar · SFCB · Bolt inclination angle · Bolt failure mode · Axial stress · Shear stress

1 Introduction

In civil and mining engineering, joints often weaken the strength of rocks and cause rocks masses to be more deformable (Li et al. 2022; Wang et al. 2022a). Fully grouted steel bolts have been widely used to reinforce jointed rock masses in the past. The type of bolts significantly affects the shear stress of jointed rock and inhibits the dislocation between rock blocks (Chen et al. 2013; Chen et al. 2014; Wang et al. 2022b). To date, most studies have focused on steel bolts and have made significant progress in understanding the rock

✉ Gang Wang
wanggang1110@gmail.com

1 Shandong Provincial Key Laboratory of Civil Engineering Disaster Prevention and Mitigation, Shandong University of Science and Technology, Qingdao 266590, China

2 School of Civil Engineering, Fujian University of Technology, Fuzhou 350118, China

bolting process. Conversely, the shear behavior of resin-reinforced composite rock bolts has received little attention, despite that it plays a significant role in the reinforcement of jointed rock masses.

Resin-reinforced composites are increasingly being used in geotechnical engineering. In previous studies, glass fiber composite bolts were used to reinforce rock masses, and the mechanical properties of the bolts under loading conditions were studied (Benmokrane et al. 2017; Wang et al. 2018a, b). Ludvig (1983) performed shear tests on Swellex bolts, steel bolts, and fiberglass bolts. Li et al. (2016) experimentally compared the shear behaviors of fiberglass bolts, rock bolts, and cables to understand the contribution of bolts to the shear strength of concrete surface and failure modes. In recent years, there has been a growing interest in using basalt fibers as a reinforcement material due to the physico-chemical and mechanical properties of basalt products, as well as the cost efficiency of production (Monaldo et al. 2019). Basalt fiber-reinforced polymer (BFRP) bars and steel–FRP composite bars (SFCBs) offer high strength, exceptional corrosion resistance, and excellent insulation. They have a great potential to replace steel bolts. Tang et al. (2020) pointed out that the BFRP bar-reinforced tunnel arches with excellent corrosion resistance can be serve as underground waterfront protective structures. Ge et al. (2015) noted that the bonding strength between BFRP bars and concrete is similar to that of steel bars and concrete, which is consistent with the findings of shows good bond performance, also Okelo et al. (2005) and Tao et al. (2014). Zhao et al. (2021) found that anchor bolts developed with BFRP have application potential in tunnels. They also used meso-scale numerical simulations and laboratory tests to examine the structural parameters of BFRP anchor plates and rods and the critical anchorage length of BFRP cement mortar anchors. As new composite materials, BFRP bars and SFCBs could replace traditional steel bolts in reinforcing rocks. However, studies on the shear behavior of jointed rocks reinforced by BFRP bars and SFCBs have been rarely reported, far behind the application.

Furthermore, although fiber-reinforced polymer is a relatively high-strength, lightweight, and long-lasting alternative to steel bars, its use in concrete construction is still limited. The stability of BFRP-reinforced structures has been the subject of numerous studies. For instance, Micelli et al. (2018) pointed out that FRP-reinforced concrete structures endure more significant deformation due to low elastic modulus and exhibit linear elastic behavior without ductility. BFRP under shear orthotropic, and the shear capacity of general BFRP-reinforced concrete is lower than that of steel-reinforced concrete due to the lower axial stiffness of FRP reinforcement (Tomlinson 2015). In addition, Su et al. (2021) claimed that the total cumulative dissipated energy of the SFCB RC beams is approximately the same as that of the steel RC beams. It seems that there is no consistent understanding of the force characteristics of BFRP bar and SFCB reinforcement members. Therefore, further study of the shear properties of BFRP bars and SFCBs is needed.

The rapid development of computer technology has given researchers new ways to explore the microscopic behaviors of rocks. For example, finite element cohesive models are often used in the simulation of cracks in brittle materials such as crystals and rocks. Different from the traditional finite element model, the cohesive zone model (CZM) was first proposed by Dugdale (1960) and Barenblatt (1962). It focuses more on simulating the microstructure of materials and can well describe the discontinuity of brittle materials such as rocks. CZM-FEM has been widely used in the engineering field, which can describe the bond-slip between the steel bars and the surrounding concrete, and the crack propagation in the composite plates (Qiao et al. 2008; Hawileh et al. 2013; Cameselle et al. 2018). The crack tip singularity can be avoided using this method when simulating crack initiation. By integrating with continuous and discontinuous joints, this approach can produce realistic simulation results (Zhang et al. 2019).

The shear behaviors of BFRP bars, SFCBs, and steel bar-bolted jointed rocks were investigated in this study by laboratory shear test. The shear strengths and shear stress–shear displacement curves of three different bolts are compared in detail. The effects of bolt inclination angle and normal stresses are examined. We also analyze the stability of the bolts from the perspective of energy absorption. We reveal the failure modes and mechanisms of different bolts. As anisotropic materials, BFRP bars and SFCBs are significantly different from steel bars. Therefore, we use the "engineering constant" model to reflect the anisotropy. Subsequently, the changes of axial forces and shear forces of BFRP bars, SFCB, and steel bars are discussed, and the shear mechanism is elucidated. In addition, the CZM model is used for the rock material, which reflects the damage characteristics of the bolts to the rock.

2 Mechanical Characteristics of the Bolts

Tensile strength, shear strength, and Young's modulus are the critical properties of bolts in geotechnical engineering, which affect the bolt performance in reinforcement. We investigated the tensile/shear mechanical behaviors of steel bars, BFRP bars, and steel-continuous basalt fiber bars (SFCB) using a universal testing machine, as shown in Fig. 1. To prevent premature failure of the fiber bars, steel sleeves were contacted for the protection. The mechanical properties of steel bars, SFCBs, and BFRP

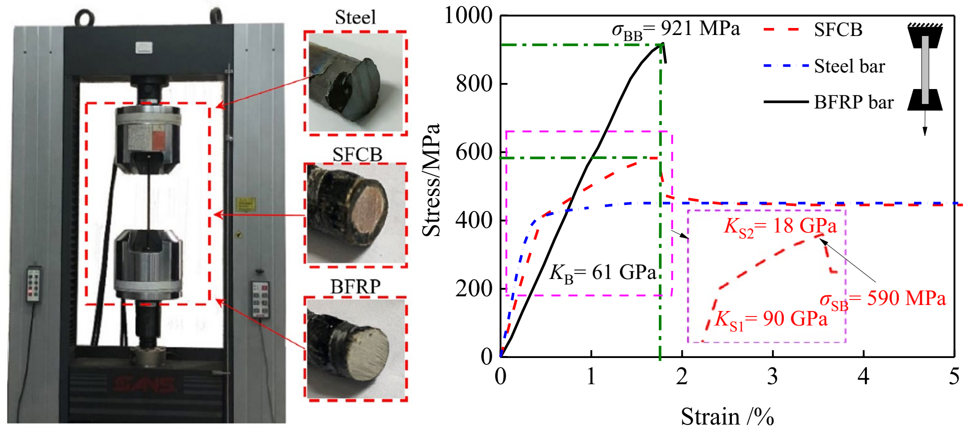

Fig. 1 Tensile test results of three different bars

bars, such as the ultimate tensile strength, and Young's modulus, vary significantly. For the SFCBs, a secondary stiffness can be identified from the stress–strain plot. Since SFCB is a composite of elastic–plastic steel and linear elastic FRP (Dong et al. 2016), the strain of the fiber is greater than the strain of the steel bar, and there exists a strain hysteresis in the steel bar. After the yielded point, the curve was similar to that of the steel bar. The results are consistent with the observations of Wu et al. (2010). For the BFRP bar, the stress–strain relationship is very close to a linear, and then its stiffness decreases slightly as the load increases until the final failure. The tensile test results show that the BFRP bar is a linear elastic material and the failure mode is brittle. It has excellent tensile properties, but the lower elastic modulus indicates insufficient material stiffness. We used the double shear test method to obtain the shear strength of the BFRP bar and SFCB, refer to JG/t406-2013 Glass Fiber-Reinforced Polymer Rebar for Civil Engineering (Beijing 2013). Table 1 lists the mechanical properties of the bolt materials.

3 Shear Experiments

3.1 Specimen Preparation

Joint molds with inclined rods were manufactured using 3D printing technology to assure the correctness of the inclination between the joint surface and the bolts. The joint model was built on a 5 mm-thick base with dimensions of 200 × 100 mm. The bolt inclination angle is defined as the angle between the bolt axis and the joint surface. According to previous studies, the bolt inclination angle was between 90° and 45°, (Cui et al. 2020; Bjurstrom 1974); hence, in this study, we selected four bolt inclination angles 90°, 75°, 60°, and 45°. The joint surface roughness follows Barton's standard roughness joint curve, with JRC 6–8 (smooth) and JRC 18–20 (rough), labeled S1 and S2, respectively. Two concrete blocks were inverted in a metal box to create the specimen. The specimens were made by combining 1:0.5:0.5:0.5 cement, fine sand, coarse sand, and water (mass ratio). Figure 2 shows the preparation process for the jointed specimens. Table 2 lists the mechanical properties of the rock-like materials.

3.2 Experimental Setup

In the tests, the constant normal load was 1–3 MPa, and the loading rate was 0.06 mm/min. Bolts with a diameter of 6 mm were made from steel bars, SFCBs, and BFRP bars. The bolt was inserted and fixed in the middle of the reserved hole, and the hole was then grouted with Portland cement (Li et al. 2021). The bolted specimens were sheared under constant normal load after solidification, as shown in Fig. 3.

Table 1 Mechanical properties of bolt materials

Bolt type	Diameter/mm	Density kg/m^3	Young's modulus/GPa	Tensile strength/MPa	Shear strength/MPa
BFPR bar	6	2010	61	921	162
SFCB	6	5640	90 (First) 18 (Second)	590	205
Steel bar	6	7800	119	451	227

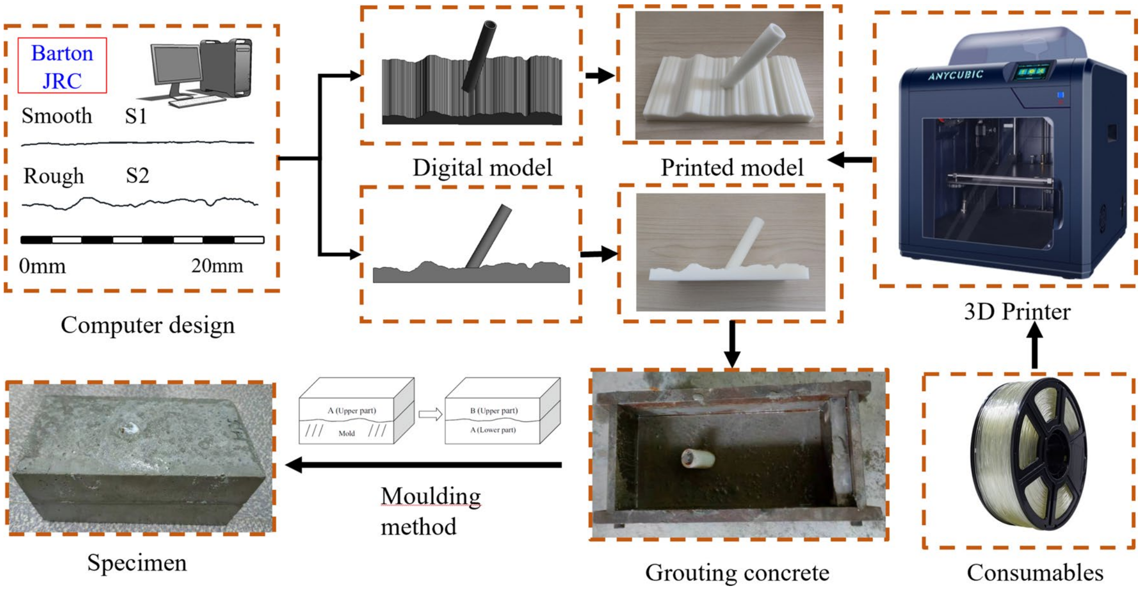

Fig. 2 Preparation process for the jointed specimens

Table 2 Mechanical properties of the rock-like materials

Type	Density (kg/m^3)	Compressive strength (MPa)	Tensile strength (MPa)	Young's modulus (GPa)	Friction angle (°)
Rock-like material	2079	32.40	2.74	41.50	34

4 Experimental Results and Discussion

4.1 Relationship Between Shear Displacement and Shear Strength

Figure 4 shows the shear stress–shear displacement curve of jointed rocks reinforced by three different bolt materials. Figure (a)–(f) represents different roughness and normal strength conditions. Table 3 shows the results of shear stiffness and energy of specimen, in which "HB" stands for

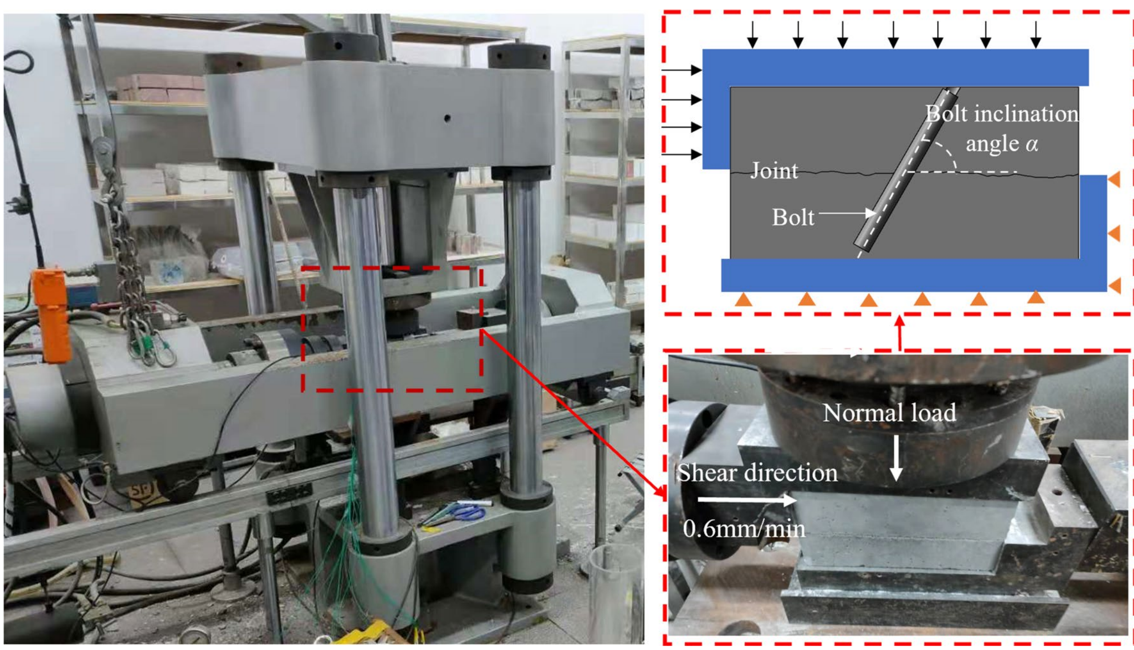

Fig. 3 Servo-controlled direct shear apparatus

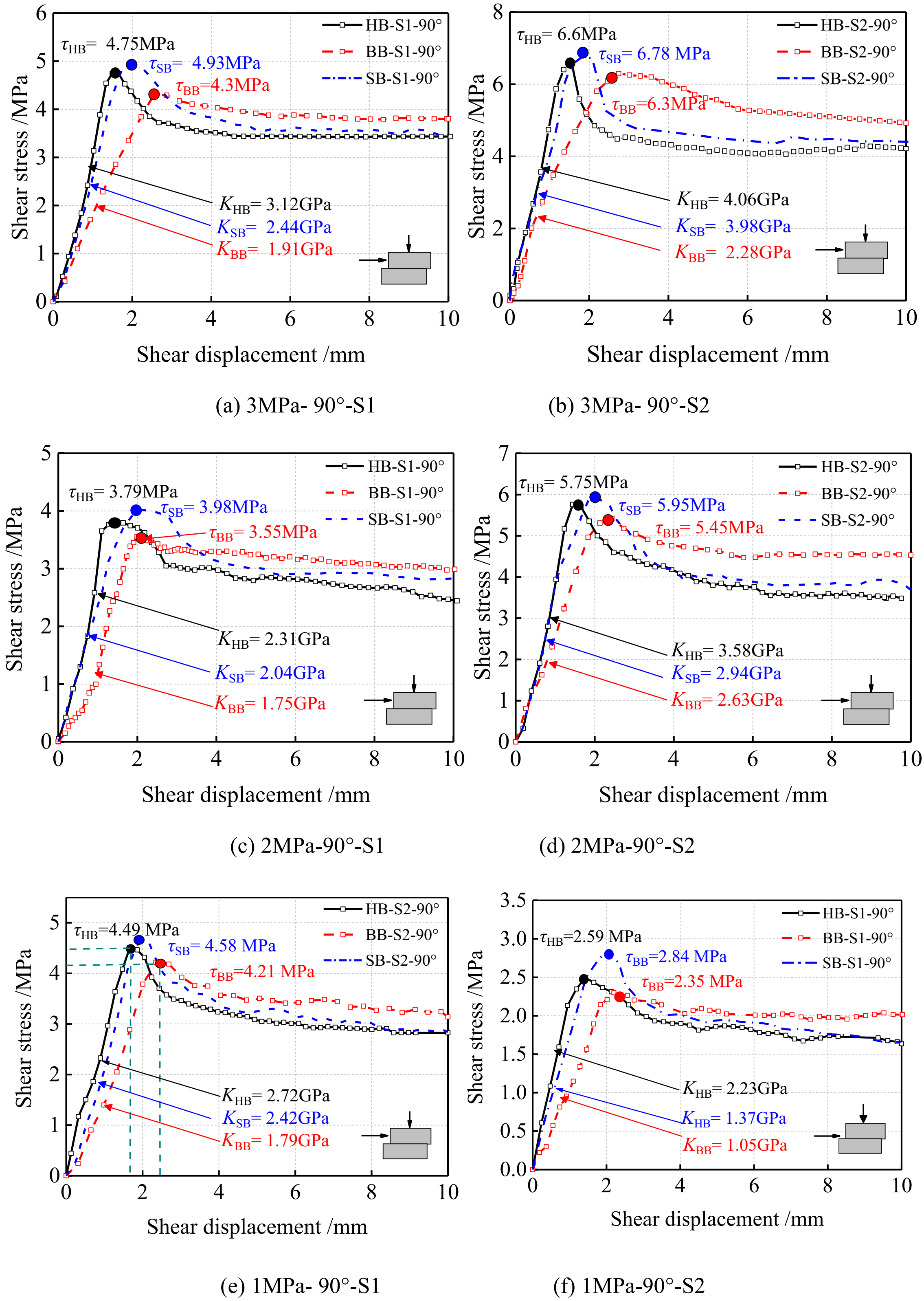

Fig. 4 Shear stress–shear displacement curve of jointed rocks reinforced by three different bolt materials

steel bolt, "SB" stands for SFCB bolt, and "BB" stands for BFRP bolt. The peak strength of the jointed rock is related to the roughness of the joint surface. As can be seen from Fig. 5, the complete shear stress–shear displacement curve of the bolted specimen can be divided into four stages: linear elastic stage, pre-peak nonlinear stage, post-peak nonlinear softening stage, and residual strength stage.

For the SFCB bolted specimens, shear stress increases rapidly with the increase of shear displacement in the linear elastic stage. After the bolt is yielded and the roughness of the joints is worn out, the specimen quickly enters the residual strength stage. The apparent characteristics are that of the pre-peak nonlinear stage and the post-peak nonlinear softening stage have a short duration, with a large range of stress changes. This is due to the presence of a steel core in the SFCB, which acts as a “pin” and increases the shear stiffness. The deformability of the outer FRP and matrix is low. When the specimen enters the residual strength stage, most of the outer surface has been loosened or ruptured, and the inner core of the steel bar plays the main role in shear resistance.

For BFRP bar bolted jointed specimens, the curve before the pre-peak nonlinear stage increases linearly. As the shear displacement increases, the shear strength decreases slowly, exhibiting a nonlinear trend during a long period of shearing. The lower stiffness degradation of BFRP material allows for a high post-peak shear load, further improving the shear strength in the residual strength stage. Because when the specimen reaches the peak load, a large number of fibers at the dislocation of the joint surface can be fully extended, and the fibers absorb a large amount of energy during shearing. Therefore, BFPR bolted joint specimens exhibit the characteristics of delayed shear strength reduction. The slow decrease in shear stress is due to the continuous accumulation of fiber slip and material damage inside the matrix.

Shear stiffness is an important parameter to characterize the shear deformation capacity of rock joints, defined as the ratio of shear stress to shear displacement. The shear stiffness of the bolted jointed specimen consists of two parts: the shear stiffness of the rock joint and the additional shear stiffness caused by the bolt dowel effect. In this work, the shear stiffness is calculated using the peak secant method, i.e., measured by the secant line between zero and peak shear stress Goodman (1970). To illustrate the effect of different bolts on the shear stiffness, we calculated and compared the shear stiffness of BFRP bars, SFCBs, and steel bar-bolted specimens.

Compared to steel bar, BFRP bar has lower shear stiffness in the linear elastic stage and larger displacement to reach the peak stress. Under different normal stresses, the shear stiffness of BFRP bar bolted specimens is only 47–73% that of the steel bar, with an average of 59%. Due to the low elastic modulus of the BFRP bar and the low shear strength of the resin matrix, the shear stress generated under the same shear displacement is lower.

The initial shear stiffness of the SFCB bolted specimens is similar to that of the steel bars, but slightly reduced. Because the inner core steel bar plays an essential role in transverse shearing, the shear stiffness is similar to that of

Table 3 Shear stiffness and energy of specimen

Specimen number	Shear stiffness *K*/GPa	Difference of the residual strengths between BB and HB /MPa	Difference of the residual strengths between SB and HB/MPa	Pre-peak energy / kN·mm	Post-peak energy / kN mm	Total energy / kN mm
HB-S1-90°-3 MPa	3.12	0.24	0.08	72.32	690.92	763.24
SB-S1-90°-3 MPa	2.44		0.08	99.62	672.64	772.26
BB-S1-90°-3 MPa	1.91	0.24		96.81	619.90	726.70
HB-S2-90°-3 MPa	4.06	1.18	0.2	107.29	887.68	994.98
SB-S2-90°-3 MPa	3.98		0.2	115.41	910.87	1026.28
BB-S2-90°-3 MPa	2.28	1.18		174.08	817.76	991.84
HB-S1-90°-2 MPa	2.31	0.35	0.17	62.18	525.80	587.98
SB-S1-90°-2 MPa	2.04		0.17	77.64	545.66	623.3
BB-S1-90°-2 MPa	1.75	0.35		72.01	522.13	594.14
HB-S2-90°-2 MPa	3.58	0.78		92.35	776.43	868.78
SB-S2-90°-2 MPa	2.94		0.3	120.43	777.68	898.11
BB-S2-90°-2 MPa	2.63	0.78		115.44	791.28	906.72
HB-S1-90°-1 MPa	2.23	0.18	0.09	30.08	361.50	391.58
SB-S1-90°-1 MPa	1.37		0.09	58.85	344.21	403.06
BB-S1-90°-1 MPa	1.05	0.18		52.60	337.64	390.24
HB-S2-90°-1 MPa	2.72	0.42	0.25	74.12	583.61	657.73
SB-S2-90°-1 MPa	2.42		0.25	86.69	574.05	660.74
BB-S2-90°-1 MPa	1.52	0.42		99.01	551.42	650.43

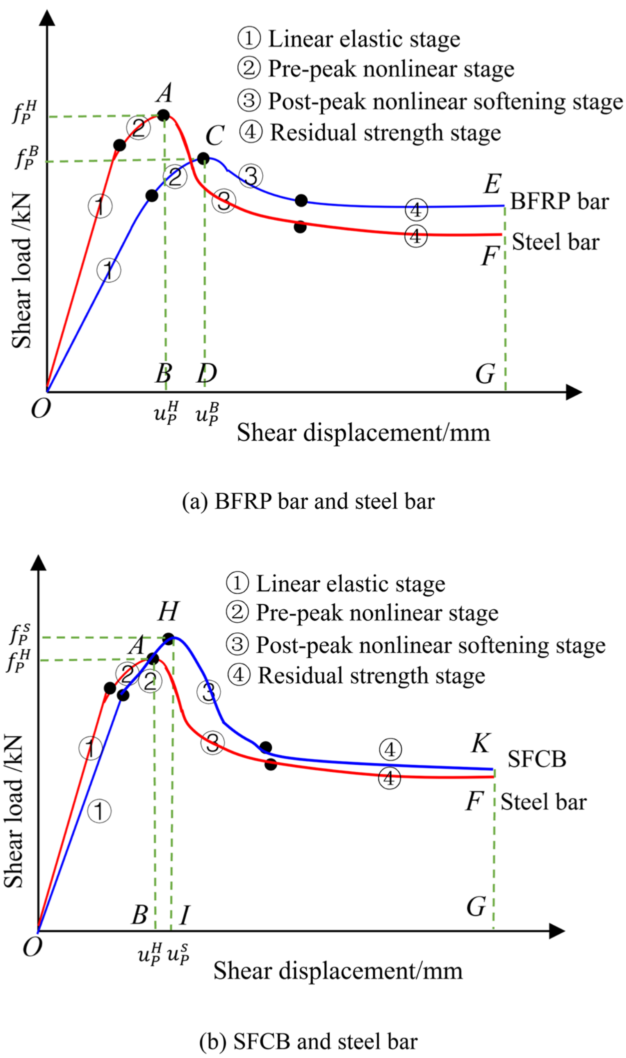

Fig. 5 Shear stress–shear displacement curves of bolted jointed rocks

the steel bar. However, the stiffness of the matrix is low, and the outer surface becomes loose after the matrix fails, resulting in a decrease in the shear stiffness of the SFCB. The shear displacement of the SFCB bolted specimen in the residual and the peak stagesis delayed compared to the steel bar bolted specimen. The reason is that after the SFCB is bent and yielded, the matrix of the FRP skin breaks, but the fibers remain and adhere to the surface of the inner core steel bar. The resistance of the fibers to axial tension inhibits the continuous deformation of the steel core, resulting in the corresponding peak and residual shear displacements being delayed. As the shear displacement increases, the matrix will break due to the increase in shear load, and the fibers will be torn by shear. In the residual strength stage, only core steel bar and residual FRP fibers provide final shear resistance. Finally, the residual stress of the SFCB is similar to that of the steel bar.

It is worth noting that although the shear stress–shear displacement curve of the SFCB is similar to that of steel bars, the SFCB has the highest peak shear strength. Since the core of the SFCB is made of steel, it has high shear strength and shear stiffness, and the skin is made of FRP fibers with strong tensile properties. Therefore, under the combination of complex shear force and axial force, SFCB can have a better resistence effect. Moreover, SFCB has a high transverse shear resistance, allowing for adequate shear stiffness and shear stress.

4.2 Toughness Analysis

Toughness is a comprehensive index used to quantitatively describe the strength and deformation ability of the bolt material, as well as the energy consumption and damage resistance of the material. In this work, we use energy indicators to assess the toughness of bolted specimens (refer to ASTM (1997)). We take the shear peak point as the dividing point to investigate the energy absorbed before and after the peak. In Fig. 5, the area below the shear load–shear displacement curve is the energy change in shear. Area OAB represents pre-peak energy absorption of the steel bar bolted specimen, area OCD represents the BFRP bar, and area OHI represents the SFCB. Area ABFG represents the post-peak energy absorption of the steel bar bolted specimen, area CDEG represents the BFRP bar, and area HIKG represents the SFCB.

Combining with the data in Table 3, it is easy to find that the energy absorbed in the pre-peak stage of the BFRP bolted specimen is higher than that of the steel bar bolted specimen. Relative to the steel bar, the energy absorbed by the BFRP bar specimens pre-peak is increased by 25%, 38%, 27%, 20%, 13%, and 25%. This indicates that BFRP has a lower peak shear stress, but the delayed shear displacement allows it to absorb more energy during the pre-peak nonlinear stage. In addition, the total energy absorbed by the BFRP bolted specimen is roughly equivalent to that of the steel bar, and the difference is only within 10%. Considering the experimental error, we believe that the shear resistance of the BFRP bolt is also very good. Although the shear strength of SFCB-bolted specimens is higher than that of steel bars, the shear stiffness is only 70%. The total absorbed energy is close to that of the steel bar, and the difference is only within 10%.

Compared with traditional materials, basalt fibers have better tensile strength, shear strength and bending properties, therefore, they have greater energy absorption rate. As a result, they have replaced metal in some fields. The failure mode of fiber composite materials under shear load is more complex, and the sources of energy absorption include tensile, compressive, and shear failure. When subjected to shear loads, the force is transmitted in two ways. One way is along the fibers, which transmits stress through the interaction between the matrix and the interwoven fibers, in the process deforming fibers and absorbing a lot of energy. The other way is through the deformation and cracking of the matrix under load, which can also absorb some energy. In addition, as the axial load is transmitted, the interface layer between the fibers and the matrix is subjected to axial pulling. When the external load is greater than the bonding strength between the layers, debonding occurs between the fibers and the matrix, and the fibers delaminate, absorbing part of the energy. As the amount of fiber deformation gradually increases, the fibers near the joint surface reach to the ultimate tensile strength, and the fibers subsequently bend and break, absorbing a lot of energy.

4.3 Bolt Inclination Angle Effect

In this section, we discuss the effect of bolt inclination angle on shear characteristics of bolted rock joints. The bolt inclination angles of the shear specimens are 90°, 75°, 60°, and 45°. Figure 6 shows the relationship between bolt inclination angle and peak shear strength. It can be seen that when the inclination angle of the bolt becomes smaller, the shear strength of the jointed rocks decreases. Under the same bolt inclination angle, the properties of various bolt materials have similar variations. Jointed rocks with bolts embedded vertically have the highest shear strength, while they have the lowest shear strength when the bolt inclination angle is 45°. Ferrero (1995) pointed out that the optimum bolt inclination angle of jointed rocks varies greatly with different rock properties. For hard rocks, the optimal bolt inclination angle is small, otherwise, it is large. The rock-like material used in this study has a strength lower than 50 MPa and belongs to soft rock, and the results are consistent to the findings of Ferrero (1995). It shows the increased stress $\triangle(\triangle 1, \triangle 2)$ of BFRP and SFCB relative to the steel bar in Fig. 6, $\triangle$ is defined as

$$\begin{aligned} \triangle 1 &= \frac{\tau_{BB}-\tau_{HB}}{\tau_{HB}-\tau} \times 100\% \\ \triangle 2 &= \frac{\tau_{SB}-\tau_{HB}}{\tau_{HB}-\tau} \times 100\% \end{aligned}, \quad (1)$$

where τ_{BB}, τ_{HB}, and τ_{SB} are the shear strengths of rock joints reinforced with BFRP bar, steel bar, and SFCB, τ is the shear strength of the no bolted rock joints.

For the BFRP bar, there is a large correlation with the bolt inclination angle. $\triangle 1$ decreases with increasing of the bolt inclination angle and are linearly related to the bolt inclination angle. In addition, $\triangle 1$ is positive when the bolt inclination angle is 45–60° and is negative when the bolt inclination angle is 75–90°. It can be inferred that BFRP bars are suitable for improving the shear strength of jointed specimens at with low bolt inclination angles. Moreover, when the bolt inclination angle is 60° and 45°, the shear strength can increase by 5–46%, and 57–71%, respectively.

For SFCB, $\triangle 2$ is always greater than zero when the bolt inclination angle is 45–90°, indicating that the shear effect of SFCB is better than that of steel bars. When the bolt inclination angle is 60° and 45°, the shear strength can increase by 9–16%, and 24–31%, respectively. Therefore, when the inclination of the bolt is 60° and 45°, the reinforcement capacity of the SFCB is lower than that of the BFRP bar. The reason is that the fiber content of the SFCB is low, and the fibers on the outer surface are easy to break due to relatively low tensile strength.

In summary, the mechanical properties of the bolt material have a great impact on the shear strength. The conditions under which BFRP bars and steel bars can exert their maximum advantage are also different. The steel bar exhibits better shear resistance at high bolt angles, whereas the BFRP bar shows better shear resistance at low bolt inclination angles.

4.4 Bolt Failure Mode

Figure 7 shows the failure characteristics of bolted specimens. The failure modes of the BFRP bolts are determined by the combined behaviors of the resin matrix and basalt fibers. They can be divided into three main types: (1) resin matrix failure and fiber bending without breaking, (2) resin matrix and fiber failure, and (3) rock crushing and fiber bending. It is clear that the final deformation of the BFRP bar is small. The major shear resistance of FRP bars is contributed by the internal fibers, while the resin accounts for only 8% of the overall strength (Wang et al. 2014). Due to the low shear strength of the resin matrix, it can break under a small shear displacement. Although the resin matrix is failed earlier, the fibers can still work. The loose BFRP bolt can further withstand tensile stress caused by joint dislocation in the residual strength stage, causing the shear stress to be higher than that of the steel bar. Fibers continue to accumulate damage under the combined action of tensile and shear forces until they break when the shear displacement is very large.

The shear failure mode of the SFCB includes two types: SFCB bending failure, and SFCB bending failure with rock crushing. Combined with the shear stress–shear displacement curve, we summarize the shear failure process as follows. First, the outer FRP fibers and the steel core are jointly sheared, resulting a linear elastic deformation. As the shear displacement gradually increases, the inner steel core gets yielded, and the strain increases substantially. However, the outer FRP fibers are linear elastic material that cannot be deformed enough, resulting in strain inconsistency. Then, the shear load is increased, the outer fibers are torn and failed, and the residual shear strength is contributed by the steel

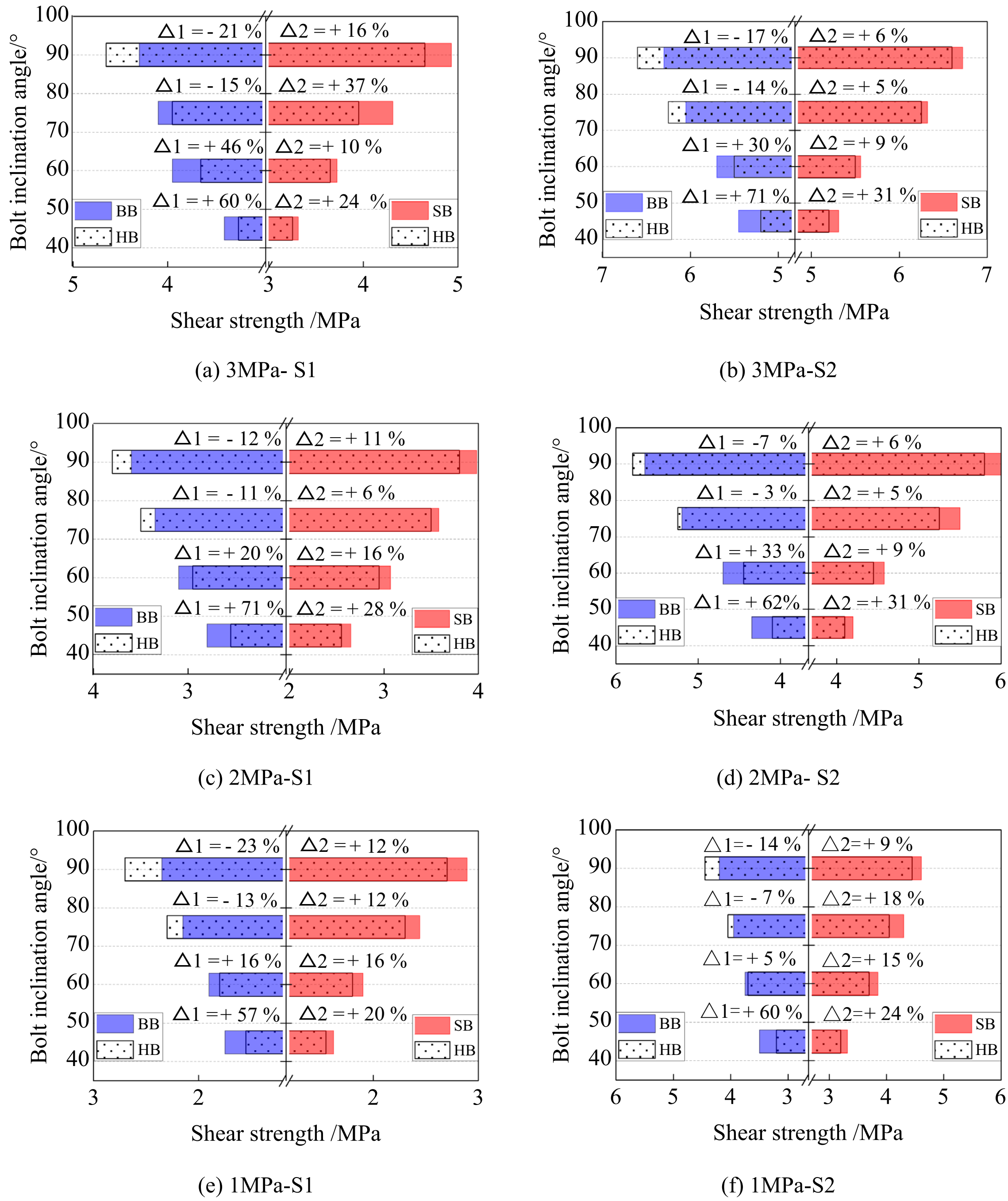

Fig. 6 The relationship between bolt inclination angle and peak shear strength

core. In addition, if the tensile stress accumulated between the fibers and the grout interface is too large, the rock will fail.

We knocked out the tested specimens and took bolts to further investigate the shear failure characteristics of different bolts. Figure 8 shows the BFRP bar and SFCB failure states. The bolts appear to be bent and deformed at the junction of the joint surface. The steel bar entered the plastic stage, and at the joint it was bent sideways by 26°. The steel bar has morphed into an "S" shape, and "plastic hinges" can be seen on both sides of the joint surface. The bending degree of the BFRP bar is only 12°, which is less than that of the steel bar. No apparent plastic yield and no "plastic hinge" is observed on the BFRP bar. The middle segment of the BFRP bar is loose and broken, the resin matrix is damaged, and several fibers are broken. SFCB is also bent into an "S" shape with "plastic hinges" with a bending degree of 23°.

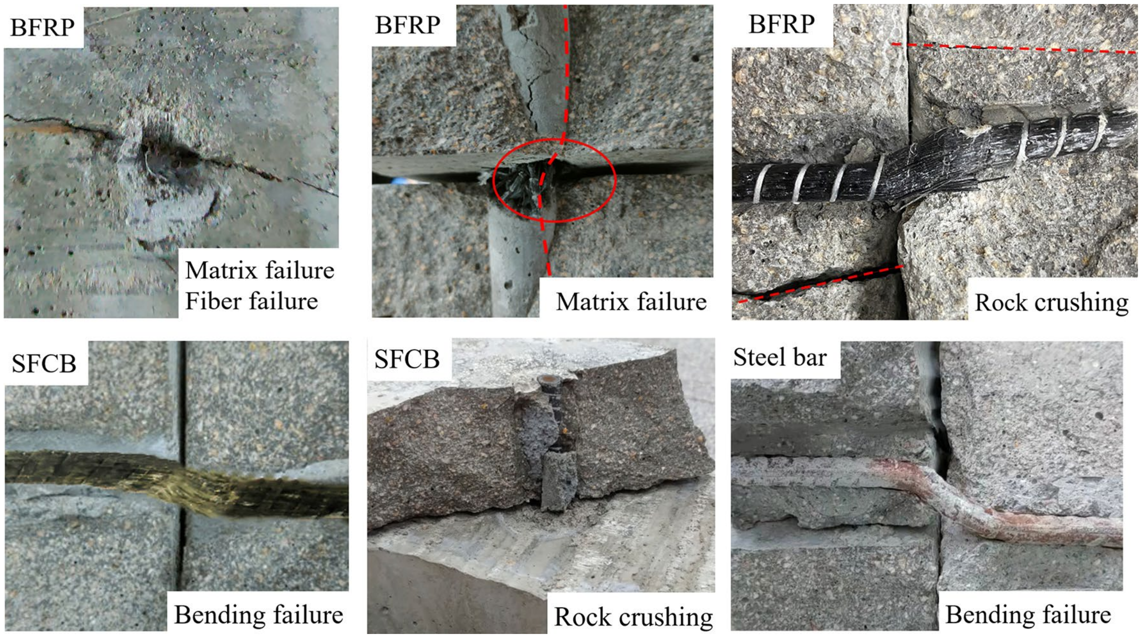

Fig. 7 Failure characteristics of bolted specimens

The outer FRP fibers are torn, the matrix is broken, and the steel core is bent into an "S" shape.

The failure mechanism of the BFRP bar and SFCB during shearing is different from that of steel bar, as shown in Fig. 9. Li and Liu (2019) pointed out that the steel bolts fail at the intersection of the bolt and the joint, and the deflection of the bolt near the joint is obvious. This indicates that failure of the bolt is due to a combination of axial and shear forces and that the bending behavior caused by the bolt dowel effect is dominant. The study of Jalalifar et al. (2006) shows similar results. Experiments show that the failure modes of the BFRP bar include pure shear and tensile fiber breakage. The shear resistance of the BFRP bar is contributed by the shear deformation of the matrix and the tensile force of the fibers. Under shear stress, the resin matrix is first damaged, and the fibers form tensile and flexural regions at the joint surfaces. As the dislocation displacement of the joint surface increases, fibers gradually break. The failure of the steel core in the SFCB is due to a combination of axial and shear forces, and the bending behavior caused by the bolt dowel effect still dominates. The outer fibers and the matrix at the joint are subjected to high shear force. In addition, fibers and the matrix are attached to the steel bar and are stressed with the deformation of the steel bar. The steel bar exhibits a deflection feature under shear, and one side of the bolt is subjected to a staggered distribution of tensile and compressive forces. As a result, the matrix on the tensile zone is more severely damaged.

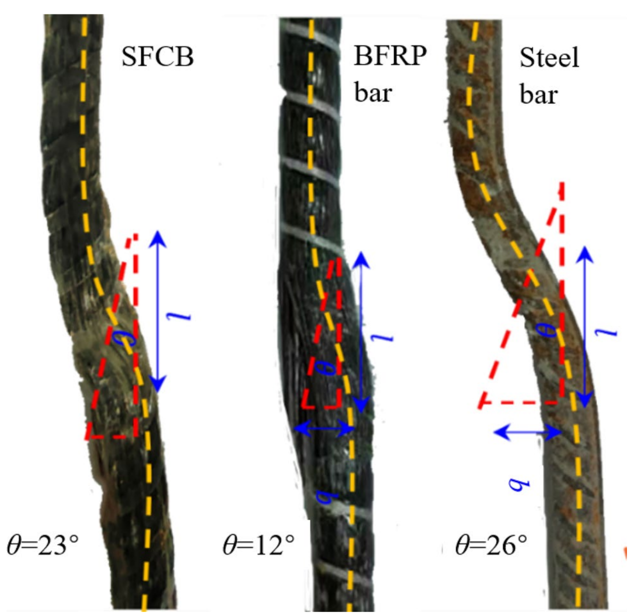

Fig. 8 Failure modes of the three different bolts

The interaction and deformation of the bolt and the grout are quite complex. The interaction mainly includes the extrusion effect of the bolt on the hole and the bond slip effect. The extrusion effect depends on the lateral deformation of the bolt. Due to the high stiffness and good elongation of the steel bolt, obvious plastic hinges and inflection points appear after bending. The vertical deformation (l) of the steel bar is 29.4 mm, the lateral deformation (b) is 9.85 mm, and the extrusion area of the jointed rock is relatively large. The matrix strength of the BFRP bar is low, and the loose and bent fiber bundles after extrusion are easily exposed; hence,

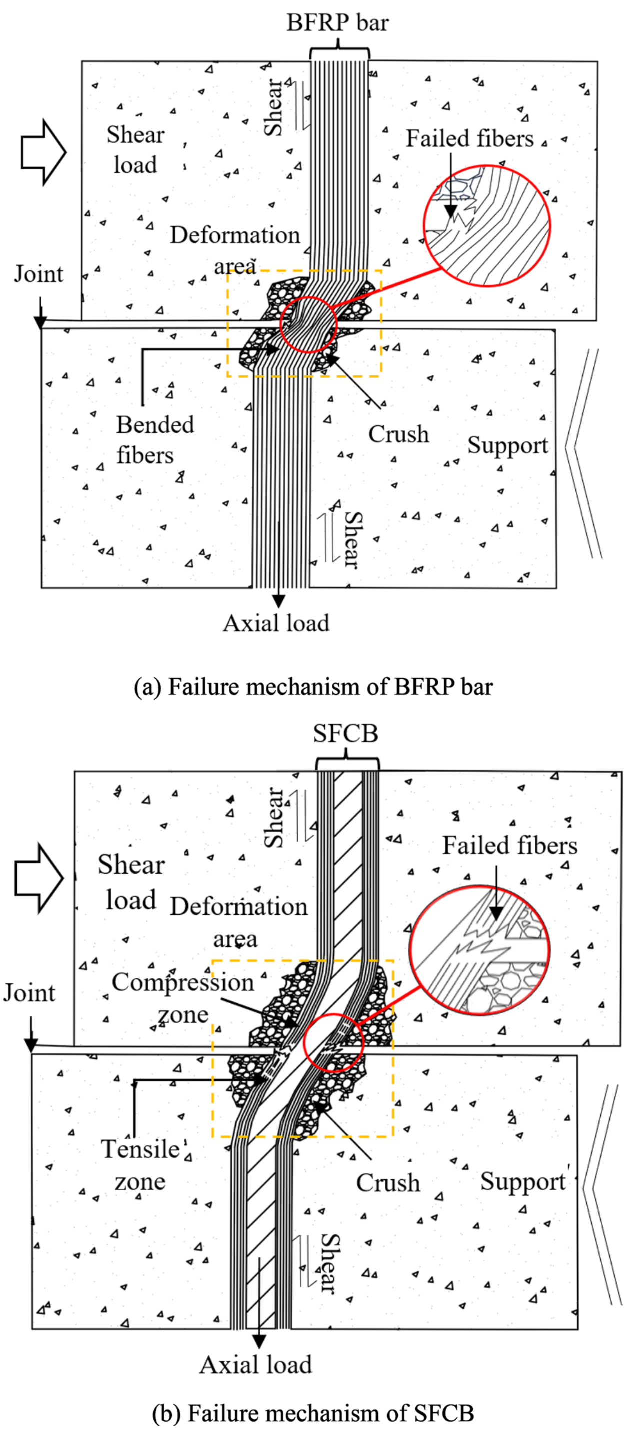

Fig. 9 Failure mechanism of BFRP bar and SFCB

the crushing zone of the hole wall and the grout is small. The vertical deformation (*l*) is 17.6 mm, the lateral deformation (*b*) is 5.84 mm, and the extrusion area of the jointed rock is small. The core of the SFCB is made of steel, which allows for the bolt to have better elongation. After bending, there are obvious plastic hinges and inflection points, and the deformation area is large. The vertical deformation (*l*) is 26.4 mm, the lateral deformation (*b*) is 8.25 mm, and the extrusion area of the jointed rock is relatively large.

The bond slip depends on the axial deformation of the bolt. During shearing, the bolt is stretched by the axial force and bond slip occurs at the bolt–grout interface. Pull-out test is widely used to evaluate bond behavior. Ge et al. (2015) found that the good bond strength between ribbed BFRP bars and concrete is similar to that of screwed steel bars of the same diameter (8 mm). In addition, there was no large slippage and pulling between the bolt and the grout, and the deformation of the bolt was concentrated near the joint surface in our experiments. It can therefore be inferred that the steel bar and SFCB may have yielded ductility and that the strain of the BFRP bar is less than or equal to the ultimate strain.

5 Numerical Simulations Based on CZM

Although the shear test can reflect the macroscopic shearing process and rock failure features, experimental observation of the rock bolt's mechanistic mechanism, particularly the interaction between the bolt and the rock interface, is highly challenging. Numerical simulation, on the other hand, has the advantage of producing a lot of details when reflecting the bolt's internal forces. The cohesive zone model (CZM) is utilized in this work to mimic discontinuities and the formation of cracks in the rock.

5.1 Bilinear Constitutive Equation in the CZM

The study is based on the traction separation criterion, which is a bilinear constitutive model. The bilinear mixed-mode softening law can be pictured in a single three-dimensional map by representing normal mode on the σ–δ_{nf} plane, and shear Mode on the σ–δ_{sf} plane, as shown in Fig. 10 (Zhou et al. 2016). This law is subject to linear elasticity before damage evolution, which can be represented by matrix:

$$t = \begin{Bmatrix} t_n \\ t_s \\ t_t \end{Bmatrix} = \begin{bmatrix} E_{nn} & E_{ns} & E_{nt} \\ E_{ns} & E_{ss} & E_{st} \\ E_{nt} & E_{st} & E_{tt} \end{bmatrix} \begin{Bmatrix} \varepsilon_n \\ \varepsilon_s \\ \varepsilon_t \end{Bmatrix} = \begin{bmatrix} k_{nn} & k_{ns} & k_{nt} \\ k_{ns} & k_{ss} & k_{st} \\ k_{nt} & k_{st} & k_{tt} \end{bmatrix} \begin{Bmatrix} \delta_n \\ \delta_s \\ \delta_t \end{Bmatrix}, \tag{2}$$

where *t* is the nominal traction stress vector, which consists of three components in 3D problems (t_n, t_s, and t_t) Where t_n $t_s$andt_t refer to the normal, the first, and the second shear stress components; ε_n, ε_s, and ε_t are the three components of the nominal strain; δ_n, δ_s, and δ_t are the corresponding separations.

In this study, the quadratic normal stress criterion is applied. It is assumed that when the quadratic interaction

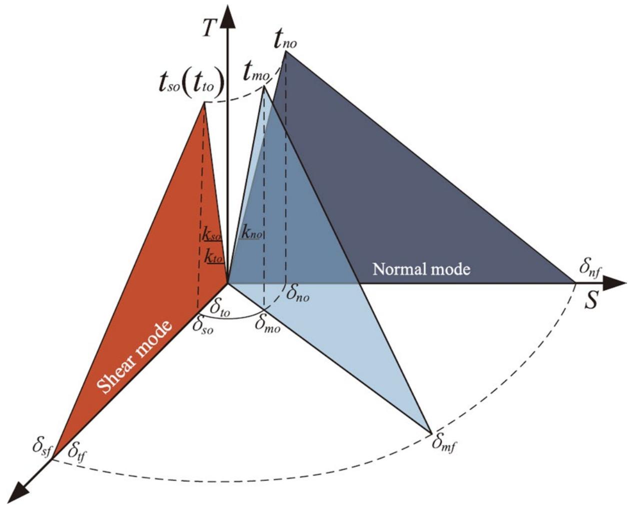

Fig. 10 Constitutive relations of the mixed-mode cohesive model

function involving the normal stress ratio reaches a value, the damage begins (ABAQUS 2017). It can be expressed as

$$\left\{\frac{\langle t_n\rangle}{t_{n0}}\right\}^2+\left\{\frac{t_s}{t_{s0}}\right\}^2+\left\{\frac{t_t}{t_{t0}}\right\}^2=1. \tag{3}$$

This method requires embedding zero-thickness cohesive elements between the initial finite element mesh (Wang et al. 2018a, b). A finite element grid with continuous overlapped surfaces is established. The mesh and nodes on the overlap surfaces are separated and the nodes are rearranged. A zero-thickness cohesive element is embedded between the original overlap element surfaces. The cohesive elements share the nodes with its adjacent mesh grids with a zero thickness. The calculated thickness can be specified manually in the ABAQUS material section.

5.2 Parameter Calibration

To obtain the accurate fracture damage parameters in the numerical simulation of jointed rock, a uniaxial compression test is simulated by CZM to measure the mechanical parameters of cohesive elements. The model adopts two types of elements: solid elements that adopt the linear elasticity criterion, and cohesive elements that adopt the traction separation criterion (Jiang et al. 2018). The Brazilian disc splitting test, shown in Fig. 11, is used to determine the simulated tensile strength. The cylindrical compression test, shown in Fig. 12, was used to check the simulated shear strength. The numerical simulation findings correspond well with the test results, and the failure patterns are also similar, indicating that these parameters can be utilized to simulate shear tests. Table 4 is mechanical parameters used in the numerical simulations.

Engineering constant models are widely used to represent the anisotropy of composites (Zhan et al. 2018). The bolt adopts the "engineering constant model", which can reflect the stiffness and yield strength in different directions, and the mechanical properties of different bolt materials are listed in Table 5 (Dtt et al. 2021). Engineering constant model is also divided into an elastic stage and a plastic stage, where the elastic stage is an orthotropic equation

$$\begin{Bmatrix}\varepsilon_{11}\\ \varepsilon_{22}\\ \varepsilon_{33}\\ \gamma_{12}\\ \gamma_{13}\\ \gamma_{23}\end{Bmatrix}=\begin{bmatrix}\frac{1}{E_1} & -\frac{v_{21}}{E_2} & -\frac{v_{31}}{E_3} & 0 & 0 & 0\\ -\frac{v_{12}}{E_1} & \frac{1}{E_2} & -\frac{v_{32}}{E_3} & 0 & 0 & 0\\ -\frac{v_{13}}{E_1} & -\frac{v_{23}}{E_2} & \frac{1}{E_3} & 0 & 0 & 0\\ 0 & 0 & 0 & \frac{1}{G_{12}} & 0 & 0\\ 0 & 0 & 0 & 0 & \frac{1}{G_{13}} & 0\\ 0 & 0 & 0 & 0 & 0 & \frac{1}{G_{23}}\end{bmatrix}\begin{Bmatrix}\sigma_{11}\\ \sigma_{22}\\ \sigma_{33}\\ \sigma_{12}\\ \sigma_{13}\\ \sigma_{23}\end{Bmatrix}. \tag{4}$$

In Eq. (4), σ_{ij}, ε_{ij}, γ_{ij} represent the stress and strain components, respectively; E_1, E_2, E_3 represent the elastic moduli in three orthogonal directions, respectively; G_{12}, G_{13}, G_{23}, respectively, represent the shear modulus in the corresponding orthogonal plane; v_{ij} represents the Poisson's ratio of the material, and $v_{\mathrm{ij}}/E_i = v_{\mathrm{ij}}/E_j$.

In the plastic yielding behavior, the yield strength coefficient in different directions can be defined by the following Eq. (5)

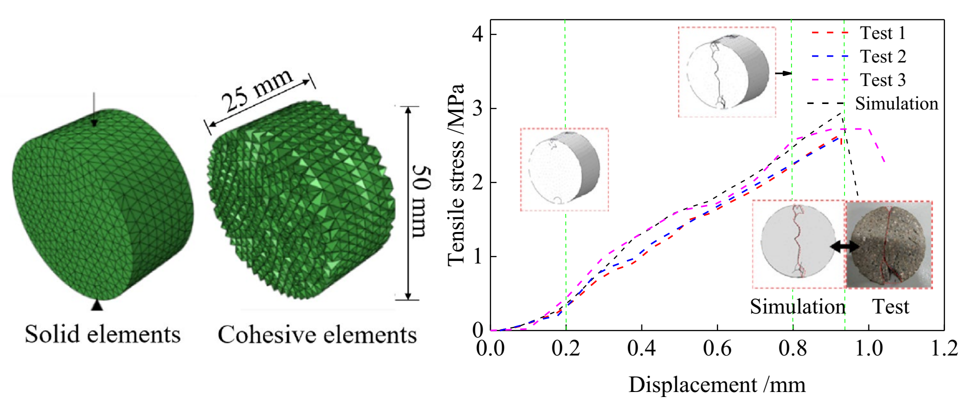

Fig. 11 Numerical models and Brazilian disc splitting test results

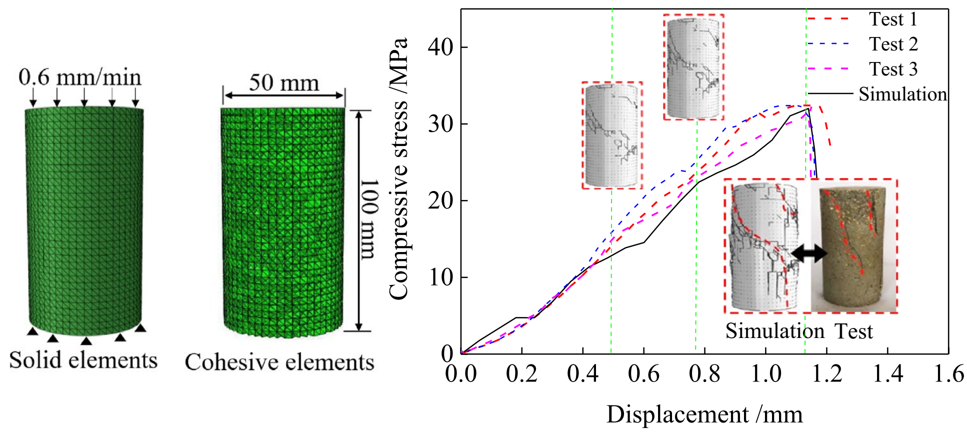

Fig. 12 Numerical models and cylinder compression test results

$$R_{11}=\frac{\tilde{\sigma}_{11}}{\sigma^0};R_{22}=\frac{\tilde{\sigma}_{22}}{\sigma^0};R_{33}=\frac{\tilde{\sigma}_{33}}{\sigma^0}$$
$$R_{12}=\frac{\tilde{\sigma}_{12}}{\tau^0};R_{13}=\frac{\tilde{\sigma}_{13}}{\tau^0};R_{23}=\frac{\tilde{\sigma}_{23}}{\tau^0}. \tag{5}$$

In Eq. (5), σ^0 is the yield stress of the material; $\tau^0=\sigma^0/\sqrt{3}$; $\tilde{\sigma}_{ij}$ is the yield strength value of each direction.

5.2.1 Numerical Model Establishment

The CZM approach is used to simulate the rock, and the continuum finite element method is used to simulate the bolt. Since the specimen is symmetrical, half of the model is analyzed. The model dimension is 100 mm high (H), 200 mm long (L), and 50 mm wide (B). We use a partition operation to obtain two material properties for the SFCB bolt, as shown in Fig. 13. The top boundary of the model is applied with a 3 MPa normal stress, the bottom boundary is completely fixed, and the horizontal displacement on the right side of the underlying rock is fixed. The "general contact" command is adopted to define contacts between all components (Zhou et al. 2015). The interaction between the bolt and the rock is connected by "tie". At a rate of 0.6 mm/min, the shear load is applied to the left side of the top rock. To mimic the properties of disordered particle distribution, we use the free meshing method. The closer the distance to the joint, the finer the mesh. There are 461,912 cohesive elements and 158,430 solid elements in the model. The software version is ABAQUS 2017, and the model of the computer is Intel(R) Core (TM) i7-6700 CPU@ 3.40 GHz.

5.2.2 Comparison Between Numerical Simulation and Experimental Results

Figure 14 shows the numerical results and experimental results of jointed rocks bolted with different bolts. The shear stress-displacement curves from the simulation are in good agreement with the laboratory tests, which suggests the validity of the simulation. Cracks from both laboratory tests and numerical simulations appear around the joint surface in the bolted specimen, which shows the accuracy of the CZM method in describing rock damage.

5.2.3 Internal Force of Bolts

Systematic analysis of bolts is important for evaluating bolting effects. Due to the complex stress states of bolts during shear, tension and compression zones are usually distributed alternately. This is consistent with the findings of Jalalifar et al. (2006). Figure 15 shows the axial force of the different bolts. The axial force of the steel bar is symmetrically distributed around the center close to the joint surface. Axial forces at both ends of the bolt are smaller and larger near the joint plane, with a maximum axial force of 4.99 kN. This indicates that one side of the bolt is subjected to compressive stress and the other side is subjected to tensile stress. As the shear load increases, tensile stress and compressive stress tend to increase. Because the bolt can inhibit the normal deformation of the surrounding rock to keep the rock in contact during the shear dilation, the axial force of the bolt also gradually increases.

The axial force distribution of the SFCB is similar to that of the steel bar, showing the staggered distribution of tension and compression zones. The maximum axial force of the SFCB is 5.76 kN, which is higher than that of the steel bar. Part of the shear strength of jointed rocks is provided by the normal constraint. SFCB can withstand higher normal stress than the steel bar, which is one of the reasons why SFCB has a higher shear strength than the steel bar. The axial force of the BFRP bar reaches the maximum near the joint surface, the axial force distribution on both sides is small and gradually increases with increasing shear displacement. The axial force of the BFRP bar is the largest, reaching 7.36 kN.

Figure 16 shows the contour maps of bolt axial stress, where "l" represents the shear displacement. As can be seen from the figure, the bolt is gradually bent as the shear stress increases, and the steel bar is bent into an "S" shape,

Table 4 Mechanical parameters used in the numerical simulations

Micro parameters	Cohesive element	Macro parameters	Solid element	Cohesive element
knn(GPa/mm)	41.5	Density (kg/m3)	2079	2079
kss(GPa/mm)	20.7)	Young's modulus (GPa)	/	41.5
ktt(GPa/mm)	20.7	Poisson's ratio	/	0.2
tn(MPa)	5			
ts(MPa)	17			
tt(MPa)	17			
Kic1(N/mm)	0.19			
Kic2(N/mm)	0.19			

Table 5 Mechanical properties of different bolt materials

Type	Steel bar	FRP
Density ρ (kg/m^3)	7800	2010
Longitudinal tensile modulus of elasticity E_1 (GPa)	200	61
Transverse tensile modulus of elasticity E_2 (GPa)	200	8
Transverse tensile modulus of elasticity E_3 (GPa)	200	8
Longitudinal Poisson's ratio ν_1	0.3	0.3
Transverse Poisson's ratio ν_2	0.3	0.3
Transverse Poisson's ratio ν_3	0.3	0.3
Shear modulus G_{12}	77	6
Shear modulus G_{13}	77	6
Shear modulus G_{23}	77	6
Tensile strength σ (MPa)	451	921
Shear strength τ (MPa)	227	162
Diameter (mm)	6	6

forming "plastic hinges" on both sides of the joint surface. The inner core of the SFCB has a stress state similar to that of a steel bar, and the FRP at the surface is in a passive deformation, which is in tension. When shear displacement increases, the tensile stress of the BFRP bar near the joint surface increases. Although the BFRP bar fails in the transverse shear direction, the longitudinal tensile stress does not reach the ultimate strength; hence, tensile stress is constantly transmitted to the center of the BFRP bar. This also explains why the BFRP bolt becomes loose and breaks in the middle, while the fibers remain connected. It also demonstrates that the tensile stress of the BFRP bolt provides the main contribution to the shear strength in the shear residual stage, and that the tensile stress increases as shear displacement increases, explaining the high shear strength in the residual strength stage.

As shown in the bolt shear force curve in Fig. 17, the shear force distribution of the steel bar and SFCB are similar, both of which have the highest shear force at the joint surface, and the minimum shear force is at the ends of the bolt. Shear stress increases with increasing shear displacement, indicating that the bolt segment near the joint surface is highly susceptible to shear stress. The maximum shear force of the SFCB is 5.72 kN, and it can be inferred that the SFCB plays a supporting role in shear resistance. However, the maximum shear force of the BFRP bar is 3.91 kN, indicating its weaker ability to resist transverse shear stress.

Figure 18 shows the shear displacement-shear force (right) and shear displacement-axial force (left) relationships for the three bolts. Each curve has an inflection point, indicating that the bolt has some degree of damage and that shear slippage may occur at the bolt grouting interface. Within 1 mm of the shear displacement, the axial force and shear force of the steel bar increase faster, while the SFCB increment rate is slightly slower, and the increasing rate of

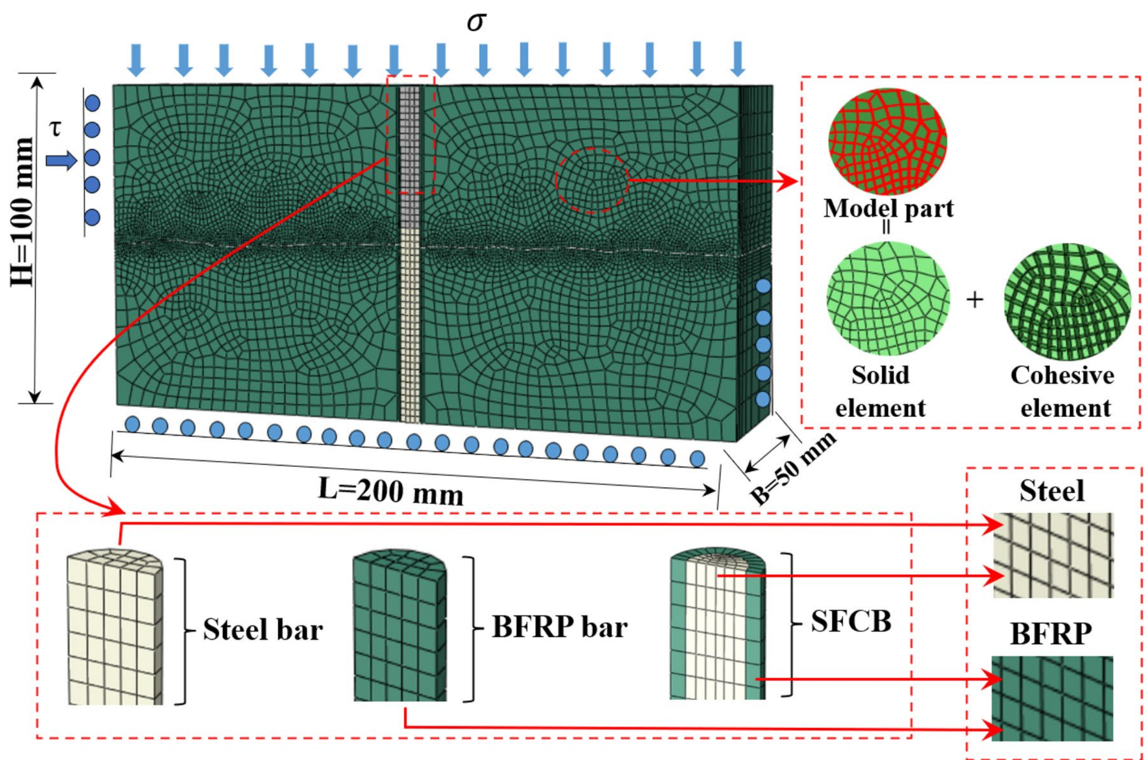

Fig. 13 Numerical model of bolted rocks

the BFRP bar is the lowest. After the displacement is greater than 1 mm, the axial force growth of the steel bar and SFCB becomes slower. In contrast, the axial force growth of the BFRP bar does not slow down until the shear displacement is greater than 2 mm. However, the shear stress growth rate of the BFRP decreases in the shear displacement range of 1 mm.

5.2.4 Effect of Bolt Inclination Angle

In this section, we analyze bolted joints with bolt inclination angles of 45°, 60°, 75°, and 90°. The relationship of normal displacement and shear displacement of the jointed rock is shown in Fig. 19. When the bolt inclination angle is increased from 45° to 90°, the maximum normal displacement is reduced from 1.02 to 0.68 mm, a decrease of 33.3%. This suggests that the normal displacement decreases gradually as the inclination of the bolt increases, which is similar to the findings of Cui et al. (2020). The normal displacement of the BFRP bar is 0.83 mm, while the shear displacement of the SFCB is 0.73 mm. Compared to the steel bar, the maximum normal displacement of BFRP bar bolted rocks is increased by 22%, while the maximum normal displacement of the SFCB bolted rocks is increased by 7%. The usage of BFRP bolts will increase the normal displacement due to the low elastic modulus.

The shear mechanical properties of the jointed rock are greatly affected by the bolt inclination angle. Diffident bolt inclination angles change the contribution proportion of the axial force and shear force to the shear strength. Figure 20 shows the variation in shear and axial forces as a function of bolt inclination angle. The contribution proportion of the axial force to the shear strength of the joint surface gradually decreases with the increase of bolt inclination angle, whereas the contribution proportion of the shear force gradually increases. These phenomena are consistent with the existing results in the literature (Li and Liu. 2019).

It can be seen that when the bolt inclination angle is small, the shear resistance of the bolt mainly comes from the contribution of the axial force. When the bolt inclination angle is 90°, the bolt acts as a "pin", and the shear resistance of the bolt is mostly contributed by the shear force. When the bolt inclination angle of the BFRP bar is 45°, the axial force plays a dominant role in the shearing process. Its maximum axial force is 14.52 kN (45°), 8.58 kN (60°), 5.41 kN (75°), and 3.44 kN (90°) higher than the shear force, respectively.

5.2.5 Damage Evolution Analysis

Figure 21 shows the crack evolution in the BFRP bar and steel bar bolted rocks. The BFRP bar bolted rock has the

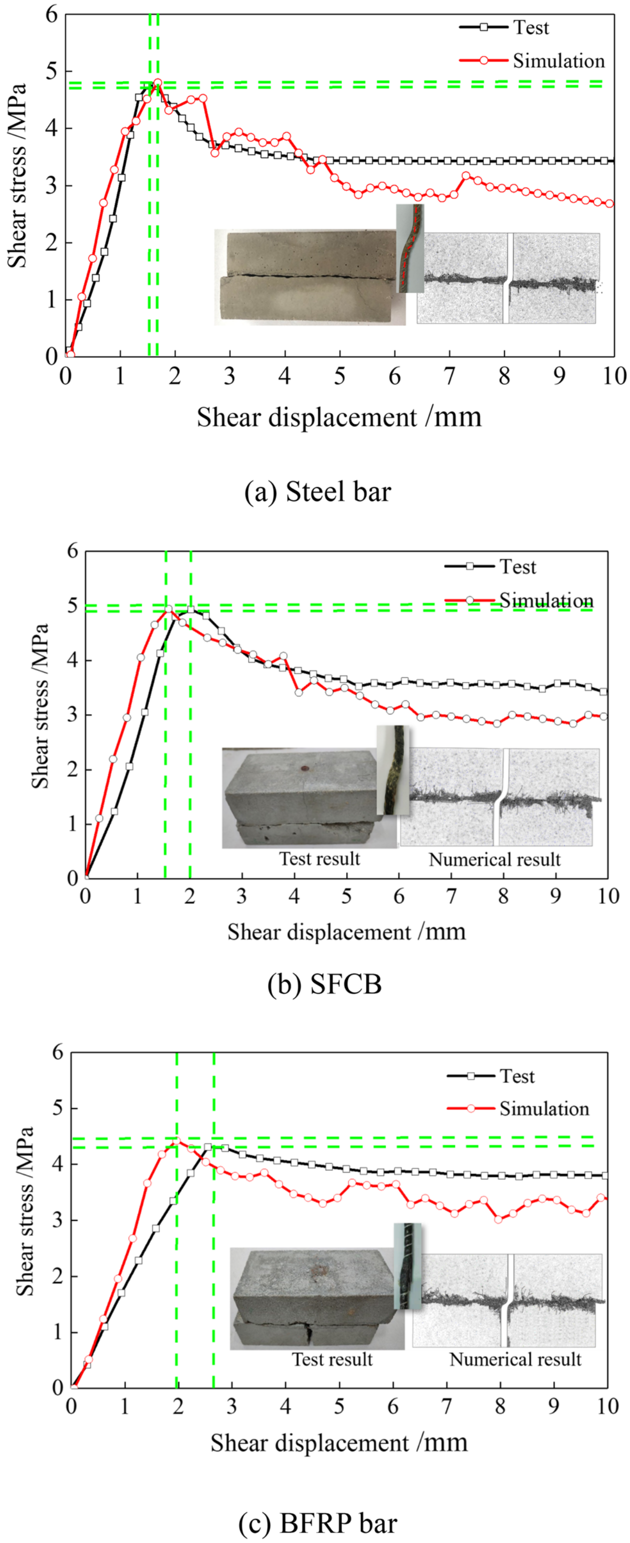

Fig. 14 Comparison of the numerical results and experimental results for three different bars

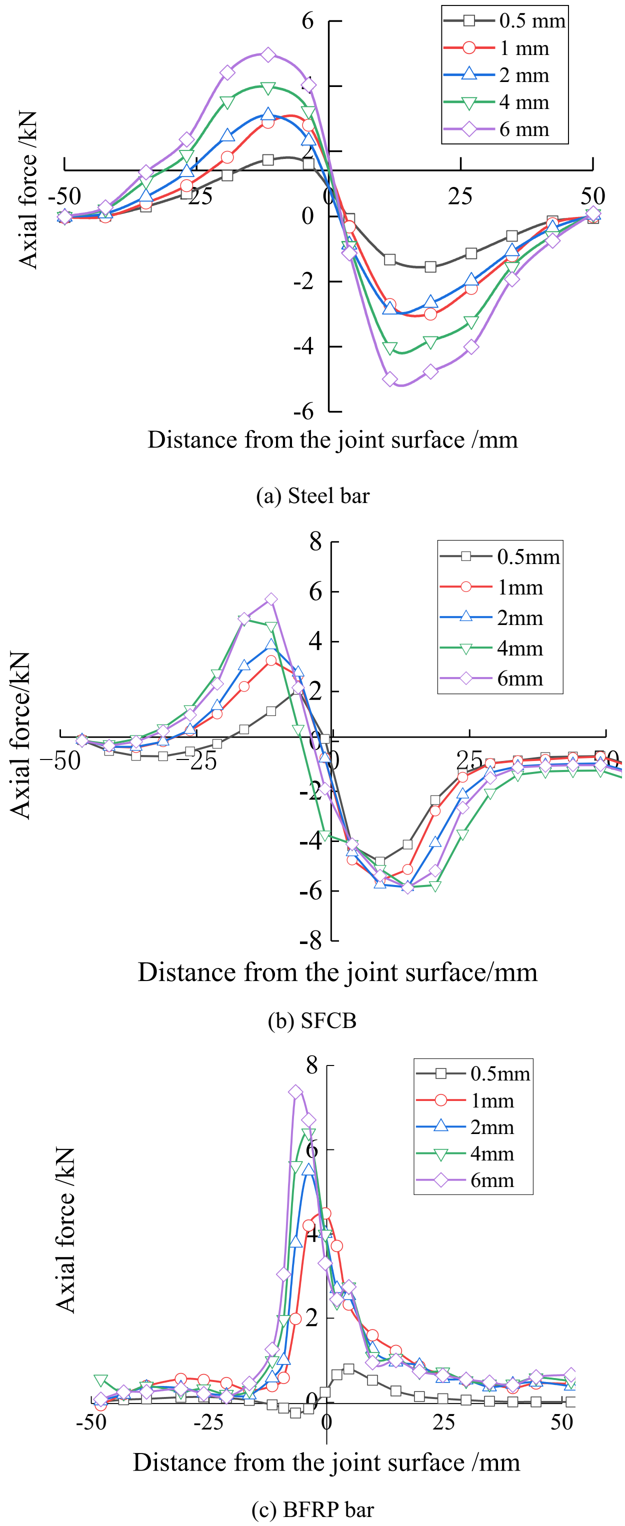

Fig. 15 Axial force as a function of distance from the joint surface

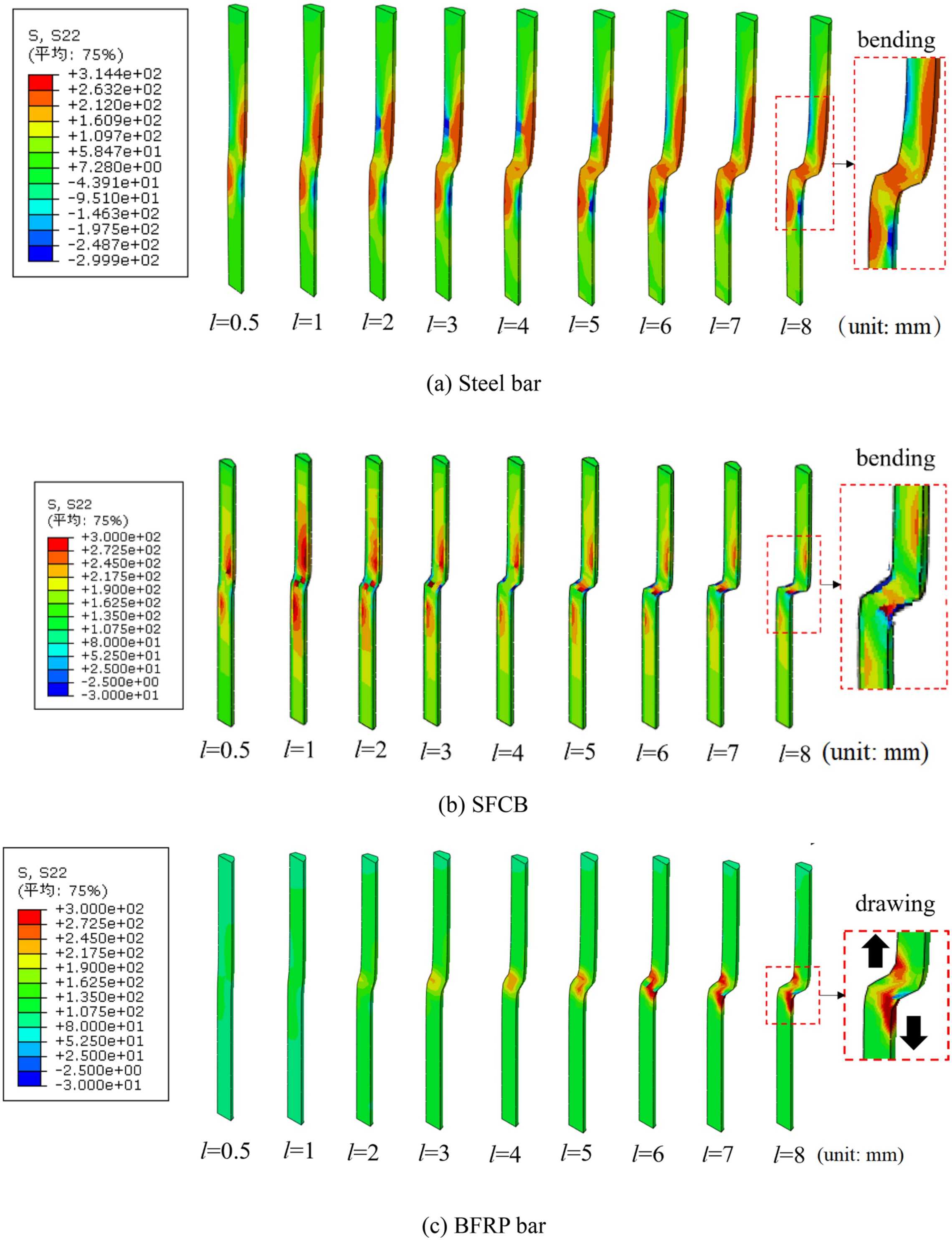

Fig. 16 Bolt axial stress contour map

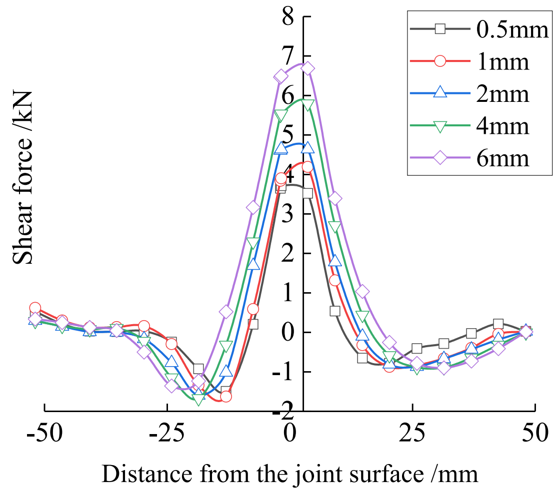

(a) Steel bar

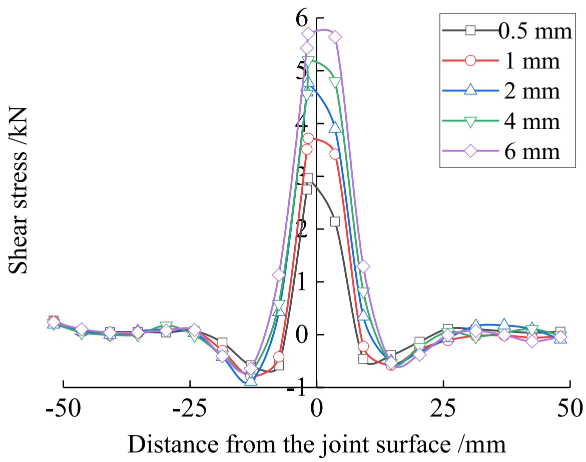

(b) SFCB

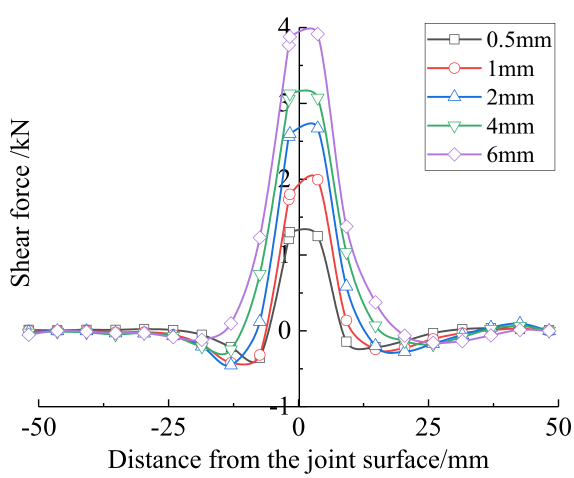

(c) BFRP bar

Fig. 17 Shear force as a function of distance from the joint surface

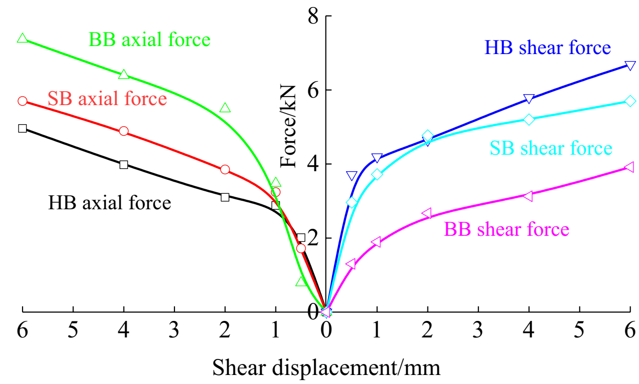

Fig. 18 Relationship between shear displacement and shear/axial force relationship for the three different bolts

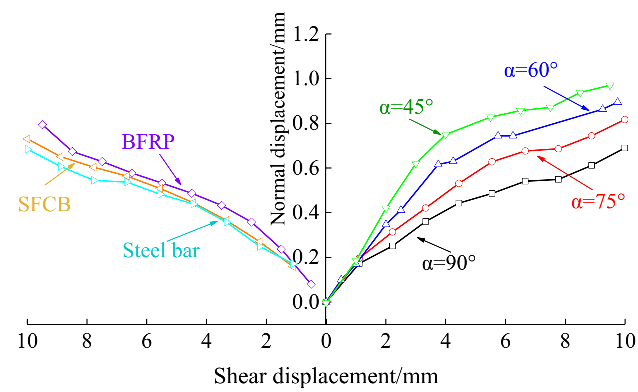

Fig. 19 Relationship between normal displacement and shear displacement for the three different bars and under four inclination angles

highest number of shear cracks at 47,300, while the steel bar bolted rock has 43,300, a 9.2% difference. The maximum crack width with the BFRP bar is 9.5 mm, while the maximum crack width with the steel bar is 7.7 mm. Therefore, the fracture area of the BFRP bar bolted rock is larger than that of the steel bar bolted rock.

Figure 22 shows the crack modes in BFRP bar and the steel bar bolted rocks. Red indicates shear crack and green indicates tensile crack. It can be concluded that shear cracks are mainly distributed in the rock near the joint surface, which is caused by the shear failure of irregular asperities near the joint surface. Tensile cracks are primarily seen at both ends of the bolt, which is due to the bending deformation of the bolt.

Under shear load, the asperities on the joint surface are sheared. Shearing gradually bends and deforms the bolt, creating tensile cracks at the rock bolt interface. It is worth noting that the damaged area with the BFRP bar is bigger at the joint surface, and the shear cracks at the rock bolt interface are more widely dispersed. Based on the above analysis, we

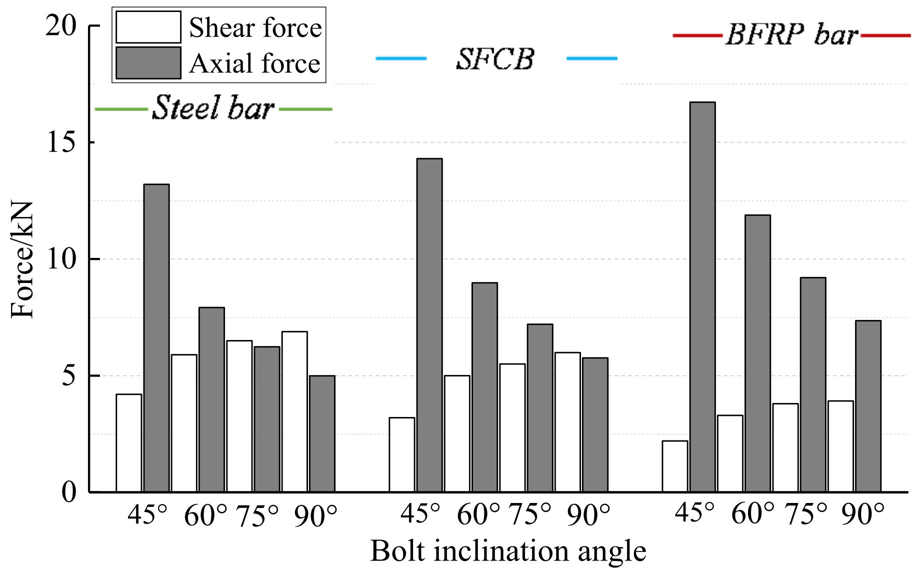

Fig. 20 Variation in shear and axial forces as a function of bolt inclination angle

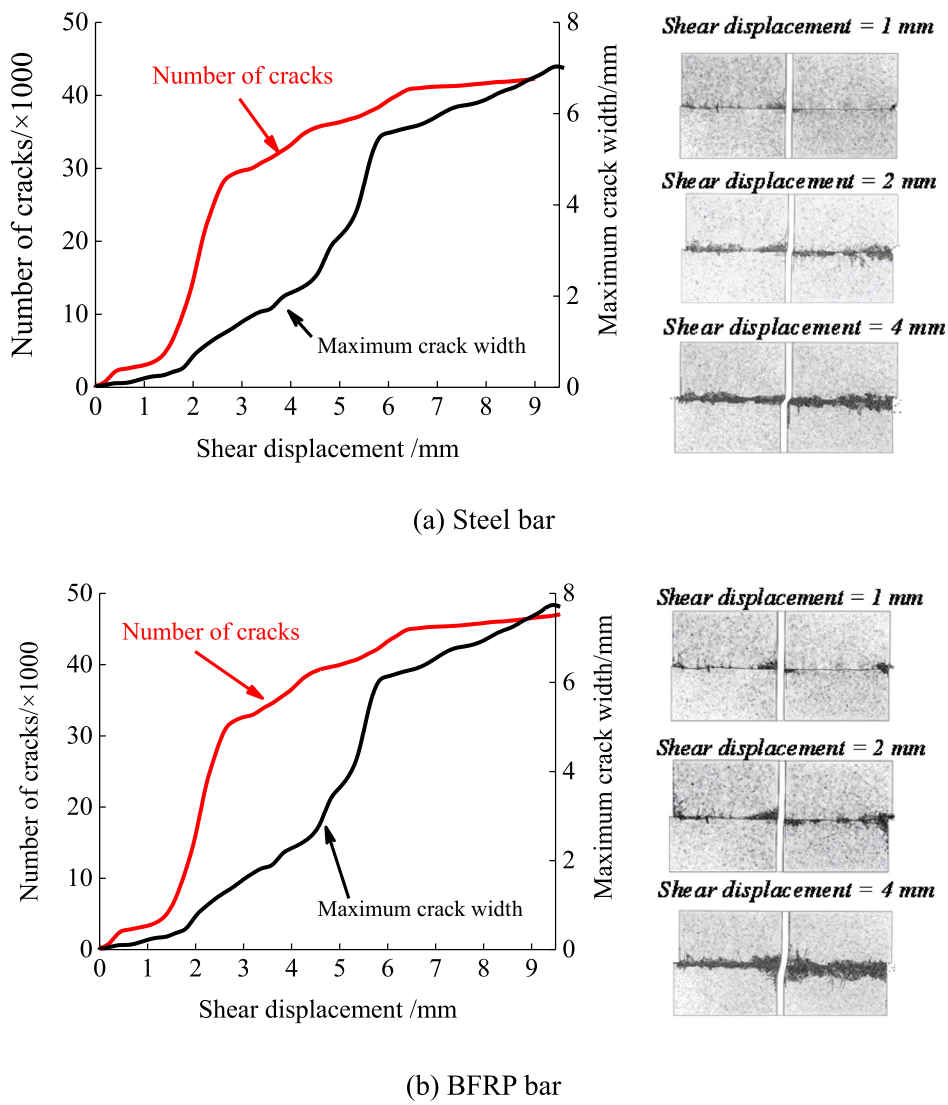

Fig. 21 Crack evolution in the BFRP bar and steel bar bolted rocks

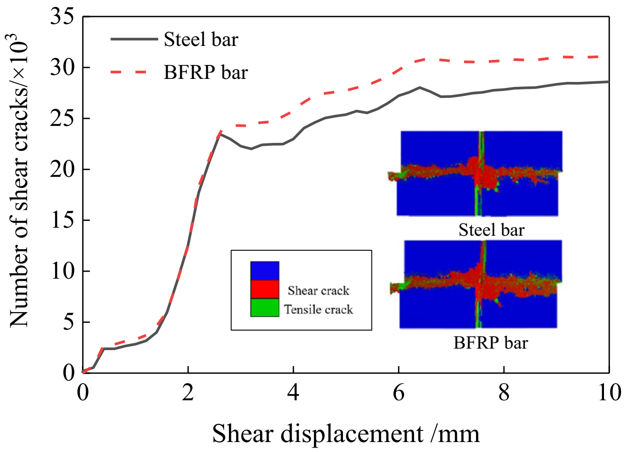

Fig. 22 Crack modes in BFRP bar and the steel bar bolted rocks

believe that the axial force of the BFRP bar has a significant impact on shear strength, which makes it easier to generate shear dislocation at the rock bolt interface.

6 Conclusions

Through experimental tests, we compared the shear properties of jointed rocks reinforced by the BFRP bar, SFCB, and steel bar. Shear strength, shear displacement, energy absorption, bolt inclination angle, and failure characteristics are all thoroughly discussed. We also used numerical simulation to examine the relationship between axial force and shear force, and crack evolution. The following conclusions can be drawn from this work.

(1) BFRP bar bolted specimens have lower shear stiffness than steel bar bolted ones in the linear elastic stage. Its shear displacement reaches peak shear stress later, but the shear stress is higher in the residual strength stage. The BFRP bar bolted specimens absorb more energy before reaching the peak shear stress. SFCBs have higher peak shear strength than steel, while the residual shear strength is the same as steel. The shear stiffness of the SFCB is slightly lower than that of the steel bar and higher than that of the BFRP bar.

(2) The shear strength of various bolted specimens is greatly affected by the bolt inclination angle. At low bolt inclination angle, the shear strengths of jointed rocks strengthened by BFRP bars are higher than that by steel bars and SFCBs. At any bolt inclination angle, the peak shear strength of the SFCB bolted specimen is greater than that of the steel bar bolted specimen.

(3) The combined action of the resin matrix and basalt fibers determines the failure mode of the BFRP bar. Matrix failure, matrix and fiber failure, and rock crushing are the three shear failure modes of BFRP bar-bolted specimens. The final deformation of the BFRP bar is small, and there is no visible plastic yield. Fiber tearing and bending failures, as well as rock crushing are the failure modes for SFCBs. SFCB failure produces “plastic hinges” and plastic yield.

(4) According to the simulation results, tensile stress contributes the most to the shear strength of the BFRP bolted specimen. At low bolt angles, it can have a greater impact. Furthermore, at the interface between the rock and the bolt, the BFRP bar is more prone to cause shear cracks and severe damage near the bolt hole.

Acknowledgements The authors would like to acknowledge financial support from the National Natural Science Foundation of China (Grant No: 52079077, 52209141); Natural Science Foundation of Shandong Province, China (Grant No.ZR2021QE069).

References

Abaqus (2017) User documentation, Dessault Systems
ASTM (1997) Standard test method for flexural toughness and first-crack strength of fiber reinforced concrete. ASTM 1018, West Conshohocken: ASTM International, 544–551.
Barenblatt GI (1962) Mathematical theory of equilibrium cracks formed in brittle fracture. Adv Appl Mech 7:56–129
Benmokrane B, Robert M, Mohamed H M, et al (2017) Durability assessment of glass FRP solid and hollow bars (rock bolts) for application in ground control of Jurong Rock Caverns in Singapore. J Compos Const 21(3):06016002.1–06016002.4
Bjurstrom S (1974) Shear strength of hard rock joints reinforced by grouted untensioned bolts. 3rd ISRM congress, Denver, USA, 1194–1199.
Cameselle Molares A, Vassilopoulos AP, Renart J, Turon A, Keller T (2018) Numerical simulation of two-dimensional in-plane crack propagation in FRP laminates. Compos Struct 200:396–407
Chen Y (2014) Experimental study and stress analysis of rock bolt anchorage performance. J Rock Mech Geotechn Eng 6(5):428–437
Chen C, Nemcik J, Ren T, Aziz N (2013) A study of rock bolting failure modes. Int J Min Sci Technol 23(1):79–88
Cui GJ, Zhang CQ, Chen JL, Yang FJ, Zhou H, Lu JJ (2020) Effect of bolt inclination angle on shear behavior of bolted joints under CNL and CNS conditions. J Central South Univ 27(03):937–950
Dong Z, Gang W, Bo X, Wang X, Taerwe L (2016) Bond durability of BFRP bars embedded in concrete under seawater conditions and the long-term bond strength prediction. Mater Des 92:552–562
Dtt A, Tmp A, Hong HB, Wc A (2021) Numerical investigation of flexural behaviours of precast segmental concrete beams internally post-tensioned with unbonded FRP tendons under monotonic loading. Eng Struct 249(15):113341
Dugdale DS (1960) Yielding of steel sheets containing slits. J Mech Phys Solids 8:100–104
Ferrero AM (1995) The shear strength of reinforced rock joints. Int J Rock Mech Mining Sci Geomech Abstr 32(6):595–605
Ge W, Zhang J, Cao D, Tu Y (2015) Flexural behaviors of hybrid concrete beams reinforced with BFRP bars and steel bars. Constr Build Mater 87:28–37
Goodman RE (1970) The deformability of joints. Determination of the in situ modulus of deformation of rock. ASTM STP 477:174–196

Hawileh RA, Naser MZ, Abdalla JA (2013) Finite element simulation of reinforced concrete beams externally strengthened with short-length CFRP plates. Compos B Eng 45(1):1722–1730

Jalalifar H, Aziz N, Hadi M (2006) The effect of surface profile, rock strength and pretension load on bending behaviour of fully grouted bolts. Geotech Geol Eng 24(5):1203–1227

JG/T 406-2013 (2013) Glass fiber reinforced polymer rebar for civil engineering. Chinese, Beijing.

Jiang HX, Meng DG (2018) 3D numerical modelling of rock fracture with a hybrid finite and cohesive element method. Eng Fract Mech 199:280–293

Li Y, Liu C (2019) Experimental study on the shear behavior of fully grouted bolts. Constr Build Mater 223:1123–1134

Li L, Hagan PC, Saydam S, Hebblewhite B, Li Y (2016) Parametric study of rockbolt shear behaviour by double shear test. Rock Mech Rock Eng 49(12):4787–4797

Li YZ, Dwayne D, Tannantc PJY, Su GS (2021) Experimental and analytical investigation of the shear resistance of a rock joint held by a fully-grouted bolt and subject to large deformations. Transportation Geotechnics 31:100671

Li JC, Yuan W, Li HB, Zou CJ (2022) Study on dynamic shear deformation behaviors and test methodology of sawtooth-shaped rock joints under impact load. Int J Rock Mech Min Sci 158:105210

Ludvig B (1983) Shear tests on rock bolts. Rock Bolting: Theory and Application in Mining and Underground Construction, Proceedings of the International Symposium on Rock Bolting, Abisko, 193–203.

Micelli F, Cascardi A, Aiello M A (2018) A Study on FRP confined concrete in presence of different preload levels. In: Proceedings of the 9th international conference on fibre-reinforced polymer (FRP) composites in civil engineering-CICE, Paris, France, 17–194.

Monaldo E, Nerilli F, Vairo G (2019) Basalt-based fiber-reinforced materials and structural applications in civil engineering. Compos Struct 214:246–263

Okelo R, Yuan RL (2005) Bond strength of fiber reinforced polymer rebars in normal strength concrete. J Compos Constr 9(3):203–213

Qiao P, Ying C (2008) Cohesive fracture simulation and failure modes of FRP–concrete bonded interfaces. Theoret Appl Fract Mech 49(2):213–225

Su C, Wang X, Ding LN, Chen ZY, Liu S, Wu ZS (2021) Experimental study on the seismic behavior of seawater sea sand concrete beams reinforced with steel–FRP composite bars. Eng Struct 248:113269

Tang Z, Zhou Y, Feng J, Liu Y, He H, Fan H (2020) Concrete protective arches reinforced with BFRP bars: construction and quasi-static structural performances. Tunn Undergr Space Technol 108(4):103731

Tao Y, Remennikov Alex M (2014) Novel hybrid FRP tubular columns for sustainable mining infrastructure: Recent research at University of Wollongong. Int J Min Sci Technol 24(3):311–316

Tomlinson DA (2015) Fam Performance of concrete beams reinforced with basalt FRP for flexure and shear. J Compos Constr 19(2):04014036

Wang X, Wang ZH, Wu ZS, Fang C (2014) Shear behavior of basalt fiber reinforced polymer (FRP) and hybrid FRP rods as shear resistance members. Construct Building Mater 73(30):781–789

Wang G, Zhang Y, Jiang Y et al (2018a) Shear behaviour and acoustic emission characteristics of bolted rock joints with different roughnesses. Rock Mech Rock Eng 51:1885–1906

Wang WJ, Song QQ, Xu CS, Gong HL (2018b) Mechanical behaviour of fully grouted GFRP rock bolts under the joint action of pre-tension load and blast dynamic load. Tunn Undergr Space Technol 73:92–91

Wang CS, Liu RC, Jiang YJ, Wang G, Luan HJ (2022a) Effect of shear-induced contact area and aperture variations on nonlinear flow behaviors in fractal rock fractures. J Rock Mech Geotech Eng. https://doi.org/10.1016/j.jrmge.2022.04.014

Wang CS, Jiang YJ, Wang G, Luan HJ, Zhang YC, Zhang SH (2022b) Experimental investigation on the shear behavior of the bolt-grout interface under CNL and CNS conditions considering realistic bolt profiles. Geomech Geophys Geo-Energy Geo-Resour 8(4):1–23

Wu G, Wu ZS, Luo YB, Sun ZY, Hu XQ (2010) Mechanical properties of steel–FRP composite bar under uniaxial and cyclic tensile loads. J Mater Civ Eng 22(10):1056–1066

Zhan Y, Liu C, Kong X, Li Y (2018) Measurement of fiber reinforced composite engineering constants with laser ultrasonic. Appl Acoust 139:182–188

Zhang SB, Wang G, Jiang YJ et al (2019) Study on shear mechanism of bolted jointed rocks: experiments and CZM-based FEM simulations. Appl Sci 10(1):62

Zhao DP, Wen SX, Wang LW, Zhang BH, Yang L (2021) Structural parameters and critical anchorage length of tunnel system bolts made of basalt fiber. Constr Build Mater 310:125081

Zhou XP, Bi J, Qian QH (2015) Numerical simulation of crack growth and coalescence in rocklike materials containing multiple pre-existing flaws. Rock Mech Rock Eng 48(3):1097–1114

Zhou W, Tang LW, Liu XH, Ma G, Chen MX (2016) Mesoscopic simulation of the dynamic tensile behaviour of concrete based on a rate-dependent cohesive model. Int J Impact Eng 95:165–175

Publisher's Note Springer Nature remains neutral with regard to jurisdictional claims in published maps and institutional affiliations.

Springer Nature or its licensor (e.g. a society or other partner) holds exclusive rights to this article under a publishing agreement with the author(s) or other rightsholder(s); author self-archiving of the accepted manuscript version of this article is solely governed by the terms of such publishing agreement and applicable law.